Kinetic Monte Carlo of transport processes in Al/AlO$_x$/Au-layers: Impact of defects

Benedikt Weiler, Tobias Haeberle, Alessio Gagliardi, and Paolo Lugli

___

Articles you may be interested in

Compression of Hamiltonian matrix: Application to spin-1/2 Heisenberg square lattice
AIP Advances **6**, 095024 (2016); 10.1063/1.4963834

Characterization of CVD graphene permittivity and conductivity in micro-/millimeter wave frequency range
AIP Advances **6**, 095014 (2016); 10.1063/1.4963140

Quantization of time-dependent singular potential systems: Non-central potential in three dimensions
AIP Advances **6**, 095110 (2016); 10.1063/1.4962995

Theoretical study of CO and O$_2$ adsorption and CO oxidation on linear-shape gold molecules (LGM$_n$) (n=2, 4, 8, 16, and 24)
AIP Advances **6**, 095206 (2016); 10.1063/1.4962824

Micro-effects of surface polishing treatment on microscopic field enhancement and long vacuum gap breakdown
AIP Advances **6**, 095103 (2016); 10.1063/1.4962549

Estimation of Curie temperature of manganite-based materials for magnetic refrigeration application using hybrid gravitational based support vector regression
AIP Advances **6**, 105009 (2016); 10.1063/1.4966043

___

Kinetic Monte Carlo of transport processes in Al/AlO$_x$/Au-layers: Impact of defects

Benedikt Weiler,[a] Tobias Haeberle, Alessio Gagliardi, and Paolo Lugli
Institute for Nanoelectronics, Technische Universität München, Arcisstrasse 21, 80333 München, Germany

Ultrathin films of alumina were investigated by a compact kMC-model. Experimental jV-curves from Al/AlO$_x$/Au-junctions with plasma- and thermal-grown AlO$_x$ were fitted by simulated ones. We found dominant defects at 2.3-2.5 eV below CBM for AlO$_x$ with an effective mass $m_{ox}^* = 0.35$ m$_0$ and a barrier $E_{B,Al/AlOx} \approx 2.8$ eV in agreement with literature. The parameterization is extended to varying defect levels, defect densities, injection barriers, effective masses and the thickness of AlO$_x$. Thus, dominant charge transport processes and implications on the relevance of defects are derived and AlO$_x$ parameters are specified which are detrimental for the operation of devices. © 2016 Author(s). All article content, except where otherwise noted, is licensed under a Creative Commons Attribution (CC BY) license (*http://creativecommons.org/licenses/by/4.0/*). [http://dx.doi.org/10.1063/1.4963180]

I. INTRODUCTION

Research on thin alumina films started already decades ago, mainly due to their usefulness for ultrathin tunneling barriers formed by insulating dielectric films of 2-3 nm thickness.[1,2] In fact, aluminum oxide, AlO$_x$, turned out to be useful for many electronic applications like silicon-on-sapphire for CMOS technology,[3] organic devices,[4] THz-nano-rectennas,[5] nTP tunnel diodes,[6] gate metals on III/V-semiconductors[7,8] and for resistive switches.[9] In these applications AlO$_x$ films are mostly produced by ALD,[7,10] RIE-plasma-growth[6] or thermal oxidation.[1]

Al/Al$_2$O$_3$/Al tunneling contacts were addressed analytically already in 1963[11] while refined models for ultrathin AlO$_x$ have been derived later on.[12] Recently, the types of defects in AlO$_x$, have been investigated, as they influence conduction pathways, like trap-assisted-tunneling (TAT) and Poole-Frenkel (PF) emission. In resistive switches they are supposed to form conductive filaments.[9,13] The charge states of defects is a critical issue in this context. Hence, density functional theory (DFT) studies, see Section III A, provide significant information on defects in AlO$_x$. However, ab initio methods have limited practical viability, e.g. to derive current densities, if multiple transport channels are present.

Therefore, we employed kinetic-Monte-Carlo (kMC) simulations in three dimensions to study charge transport through ultrathin AlO$_x$-films for MOM-applications. Our study distiniguishes from former computational studies for charge transport in oxides which solved the Poisson and Shockley Read Hall equation[14,15] or continuity equation[16–18] in one dimension. First, our compact kMC-model[19] for the current density through Al/AlO$_x$/Au-layers is introduced briefly. Second, we compare our simulations to experimental jV-data from Al/AlO$_x$/Au-junctions, where thin AlO$_x$-films were prepared by a combination of oxygen plasma and thermal treatment of the Al electrodes prior to Au deposition. From this validation we obtain a parameterization of our model, based on recent DFT-studies on defects in alumina. Third, we extensively employ the model to examine relevant parameter combinations. We vary oxide thicknesses, barrier heights, effective masses, defect densities and defect levels in up to 8-nm-thin AlO$_x$-layers to derive practical implications for AlO$_x$-growth.

---

[a]Benedikt Weiler: benedikt.weiler@nano.ei.tum.de

II. METHODS - KMC-MODEL OF Al/AlO$_x$/Au

Our kMC-model shall be briefly described here, since a detailed description and validation of our kMC-simulator can be found in Refs. 19–21. The most recent model that is best comparable to the one presented here is the statistical model reported by Vandelli et al.[22] and Padovani[23,24] for technologically promising SiO$_2$/HfO$_2$ structures. Aside from the different materials they investigate, their approach differs from ours, as they implemented interaction cross sections to derive transport rates instead of implementing and using the rates directly for the kinetic Monte Carlo algorithm here, cf. Ref. 19, which would allow for simulating also the transient behaviour of the system. Moreover, their models were one-dimensional just as the ones by Schroeder[16–18] or Novikov,[14,15] too, while our code operates in three dimensions. According to the band diagram in Fig. 1 and the summary of the simulation parameters in Table I, we included five, partly correlated, electron transport processes (holes are omitted due to the high VB offset) chosen in each simulation step after the Gillespie algorithm[25] to simulate current densities through the MOM-structures as described accurately in Ref. 19, too. There are Schottky Emission (SE), Direct Tunneling (DT), Fowler-Nordheim-Tunneling (FN), Trap-Assisted-Tunneling (TAT) or Poole-Frenkel-Emission (PF). In each step of one simulation run (consisting of at least 10.000 steps) is chosen after the Gillespie algorithm[19,25] statistically weighted by their rates. From the sum of all electrons transported to the counter electrode per time interval the total current densities through the MOM-contact is calculated. Firstly, SE, DT and FN are subsumed into the Tsu-Esaki-Formula as in Ref. 26:

$$R_{DT} = \frac{A}{4\pi^3\hbar^3} \int_0^\infty dE_x T(E_x) \times \ln\left[\frac{1 + e^{(E_{F,ca}-E_x)/k_BT}}{1 + e^{(E_{F,ca}-eV_{ox}-E_x)/k_BT}} \right]^{\frac{m_{ca}^*}{m_{an}^*}} \tag{1}$$

with $T(E)$ being the transmission coffficient for electrons to tunnel between x_0 and x_1 calculated analytically in WKB-approximation according to

$$T(E) \approx e^{\left\{ -\frac{4}{3}\frac{2m_{ox}^*}{\hbar^2}\left[\left(\phi_B - e\frac{V_{ox}}{d}x_1 - E\right)^{3/2} - \left(\phi_B - e\frac{V_{ox}}{d}x_0 - E\right)^{3/2} \right] \right\}} \tag{2}$$

where $V(x) = \phi_B - e\frac{V_{ox}}{d}x$ is the potential with V_{ox} the voltage drop over the oxide, $\phi_B = \phi_{B,Al/AlOx}$ is the barrier height between Al and AlO$_x$ and m$_{ox}^*$ is the effective mass in AlO$_x$, e is the electric charge, T is the temperature (fixed at 298 K), m_{ca}^* and m_{an}^* are the effective electron masses in the cathode (Al) and the anode (Au) respectively, which are identical here $m_{ca}^* = m_{an}^* = 1[m_0^*]$.[27] Note already that at room temperature and very high electric fields >0.1 MV/cm only FN-branches and neither SE nor DT were visible in our simulations. Furthermore, E_x is the kinetic energy of an electron and $E_{F,ca} = E_{F,Al}$ is the Fermi-level in the cathode. As sketched in Fig. 1 the Fermi level $E_{F,Al}$ (dashed line) is taken as reference point (0 eV). The conduction band offsets (CBO) $\Delta\phi_{ca}$
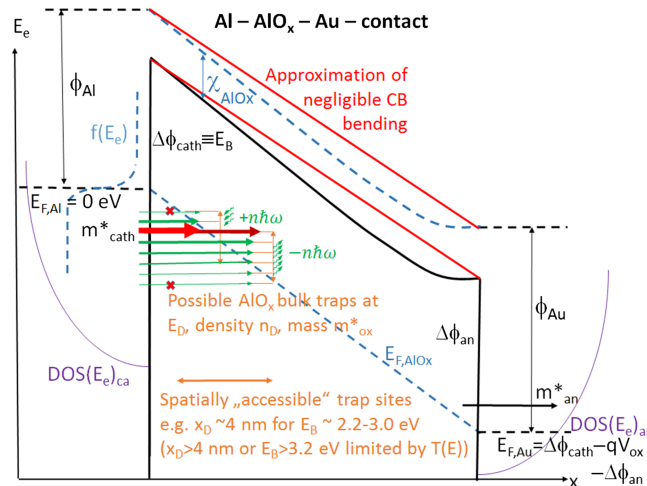

FIG. 1. Electronic band structure of Al-AlO$_x$-Au under bias modelled in kMC. Explanations in the text.

TABLE I. Physical parameters varied in the simulations for the validating fits. B: barrier, D: defect, ox: oxide.

Parameter	Reference (ab initio) value	Variation range	kMC-Fit-value # 1, d_{ox} = 5.8nm	kMC-Fit-value # 2, d_{ox}=6.7nm
$E_{B,Al-AlOx}$ [eV]	2.8-3.0	1.6-3.2	2.8	2.8
n_D [cm^{-3}]	5×10^{18}	2×10^{18}-8×10^{18}	4×10^{18}	4×10^{18}
E_D [eV]	2.0 (α-Al$_2$O$_3$), 2.8-3.0 (κ-Al$_2$O$_3$)	2.0-3.0	2.3	2.5
m_{ox}^* [m$_0$]	0.25-0.3	0.2-0.4	0.35	0.35

and $\Delta\phi_{an}$ obey Mott-Schottky-rule, determine the oxide Fermi level, cf. Ref. 19, and also $E_{F,Au}$ by assuming a linear voltage drop $V_{ox}/d \cdot x$ over the oxide.[28] Assuming a fast extraction of charge carriers from the oxide condution band to the anode, it is a good approximation that bands bend only in a negligibly small region at the anode and a linear voltage drop over the oxide is justified (red instead of black line). The contribution of the Coulomb potential due to the charge of emptied defects can be neglected in the model for AlO$_x$. Its contribution to the overall potential is just ~0.025 eV at only ~0.3 nm distance around a charged defects. Since the defect densities in all simulations were chosen smaller than $n_D \sim 0.01 nm^{-3} = 1 \times 10^{19} cm^{-3}$ the average distance between two traps was on average $n_D^{-1/3} = 3.2$ nm. Thus, the Coulombic potential of a positively charged trap will affect the tunneling barrier only on a comparably small region around the trap and it can reasonably be neglected. However, a change in physical properties like defect levels, densities, relaxation energies or dielectric properties for a different material will alter the contribution of the Coulomb potential due to charged traps. This might cause the present approximation with respect to the Coulomb potential not to be valid anymore. Moreover, also the image potential for tunneling electrons can be omitted in the first approximation, as was discussed by Weinberg[29,30] and Schenk.[31] They came to the conclusion that it is negligible to include it for electrons tunneling through a barrier which is several 0.1 eV high. The short explanation is that the image potential induced by electrons must be weighted by the probability T(E) that a tunneling electron is present in the barrier. This probability decreases exponentially with increasing barrier height. A numerical evaluation of T(E) including the full, non-weighted image potential resulted in a rather constantly ~0.15 eV higher barrier heights than in the fits. This constant value can later be simply added to the fitting parameter E_B for simulations without the image potential in Section III A. Since we have asymmetric electrodes, i.e. barriers, for the special case of tunneling to $x_1 = d$, the second barrier height ϕ_B in Equ. (2) was set to $\phi_B = \phi_{B,AlOx/Au} = 4.0$ eV. Considering TAT, first electrons are injected from Al into trap levels at E_D below CBM in AlO$_x$, either elastically (red arrows) or inelastically (green), i.e. phonon-assisted (energy $\hbar\omega$). Injection is favored for "resonance" of $E_{F,Al}$ and E_D, i.e. there is a trade-off between pre-defined trap levels E_D and (random) trap locations x_D determining the injection rates. Elastic injection (or extraction) from (into) the metallic electrodes into (from) traps is implemented after Svensson and Lundstroem:[32]

$$R_{El,D} = \frac{m_{el}^{*}{}^{5/2}}{m_{ox}^*} \left(\frac{8E_x^{3/2}}{3\hbar\sqrt{E_D}} \right) f(E_x)T(E_x) \tag{3}$$

with index $El = ca,an$, $f(E_x)$ being the Fermi-function, i.e. the probability that an electronic state in the electrode is occupied by an electron of energy E_x. Correspondingly, by the complementary probability $1 - f(E_x)$ replacing $f(E_x)$ the extraction from a trap at E_D (w.r.t. CBM) to an unoccupied state at E_x in the electrode was modelled. The defect energy E_D is modelled to be shifted to a value $E_{D,occ}$, if an empty trap gets occupied by an electron, or a value $E_{D,unocc}$, if a full trap gets unoccupied. Thus, the model can account for an energetic shift, as rationalized and reported in Ref. 20 of traps by $\Delta E_D = E_{D,occ} - E_{D,unocc}$ distinguishing further between occupied and unoccupied states via setting the two parameters $E_{D,occ}$ and $E_{D,unocc}$ to different values. However, this feature of the model was only used explicitly in Section III B, while in the other parts of this work just one value $E_D = E_{D,occ} = E_{D,unocc}$, i.e. $\Delta E_D = 0$ eV, was used. Furthermore inelastic injection rates between defect levels at E_D and the electrodes were employed including multiple-phonon-assisted-processes according to the model by Hermann and Schenk,[33] which is similar to the one

by Henry and Lang[34] as explained in earlier studies where we set up and proved the concept of our kMC-simulation code for the first time.[19,21] For reasons of brevity only the injection rates for this multiple-phonon (MP)-assisted tunneling process shall be shown here, while the extraction rates are modelled analogically and only the result shall be shown below. For the inelastic injection rates it holds:[33]

$$R_{El,D}^{MP} = \frac{1}{\tau_{El,D}^{MP}} = \int_{-\infty}^{\infty} N_{El}(E_x)f(E_x)T(E_x,x_D)\,c_{El,D}(E_x,x_D)dE_x \tag{4}$$

where $N_{El}(E_x)$ is the common DOS of the free electron gas (parabolic bands) in the electrodes and $c_{El,D}$ are capture rates for phonon absorption. Phonon emission rates are modelled analogically with a $c_{D,El}$ multiplied by $1 - f(E_x)$ in the argument. Both formulae include the multiphonon transition probability $L_m(z)$ calculated by[22,33]

$$L_m(z) = \left(\frac{1 + f_{BE}}{f_{BE}}\right)^{p/2} \exp\{-S(2f_{BE} + 1)\}\,I_m(z) \tag{5}$$

Finally, the derivation by Herrmann and Schenk results into the MP capture rates[33]

$$R_{El,D}^{MP} = c_0 \sum_{m<0}^{-\infty} N_{El}(E_m)f(E_m)T(E_m,x)L_m(z)\exp\left(\frac{m\hbar\omega}{k_BT}\right) + \\ \sum_{m>0}^{\infty} N_{El}(E_m)f(E_m)T(E_m,x)L_m(z) \tag{6}$$

and the emission rates

$$R_{DE}^{MP} = c_0 \sum_{m<0}^{-\infty} N_E(E_m)(1 - f(E_m))T_{DE}(E_m,x)L_m(z) + \\ \sum_{m>0}^{\infty} N_E(E_m)(1 - f(E_m))T_{DE}(E_m,x)L_m(z)\exp\left(-\frac{m\hbar\omega}{k_BT}\right) \tag{7}$$

They contain the Huang-Rhys factor S, the modified Bessel functions $I_m(z)$ of order m with the argument $z = 2S\sqrt{f_{BE}(1 + f_{BE})}$ and f_{BE}, the Bose-Einstein distribution giving the phonon occupation number. First, we assumed a typical Huang-Rhys factor S of 10 and a typical phonon energies of 40 meV.[35,36] This corresponds to a relaxation energy which is defined as $E_{rel} = S\hbar\omega_D$ of 0.4 eV. Note that the presented computational model allows for an independent adjustment of ΔE_D and $E_{rel} = S\hbar\omega$. The Huang Rhys factor S can be determined by fitting temperature dependent $j - T^{-1}$ curves showing a dominant MPTAT transport for low T. This was done using a comparable model by Vandelli et al. who fitted jV-curves for several temperatures,[22] however, it was out of scope of the present study. Hence, S was fixed to a value of 10, if not stated otherwise which implied that more than 10 phonons for absorption or emission are improbable, cf. Section III B. Note also that the single-mode approximation permits only energies $E_m = E_x \pm m\hbar\omega$ to appear after evaluation of the integral in Eq. (4). To complete the inelastic MP assisted rates, the prefactor c_0 is calculated under the approximation of a 3D delta-like potential of the traps[33]

$$c_0 = \frac{(4\pi\hbar eF)^2}{2m_{ox}^* E_g (2m_{ox}^* E_D)^{3/2}} \tag{8}$$

where E_g is the bandgap of the oxide and $F = V_{ox}/d$ is the electric field, as V_{ox} drops over the oxide of thickness d. Carrier transport processes between traps in AlO_x were simulated by the common Miller-Abrahams-rates (MA) according to the assumption of hopping of small, localized polarons in AlO_x:[37,38]

$$R_{ij} = \nu \exp\left\{\frac{-2r_{ij}}{r_D}\right\} \cdot \begin{cases} \exp-\frac{\Delta E}{k_BT}, & \text{if } \Delta E > 0 \\ 1, & \text{otherwise} \end{cases} \tag{9}$$

where $r_D = \frac{\hbar}{\sqrt{2m_{ox}^* E_D}}$ is the localization radius and $\Delta E = E_j - E_i$ is the difference in energy between the initial and final defect. As last transport process implemented electrons captured in an initially

positively charged trap can be emitted by field-assisted PF-emission according to the 3D-PF-emission formulas first derived by Hartke *et al.* in Ref. 39:

$$R_{PF} = \nu \cdot \exp\left\{ -\frac{1}{k_B T}\left(E_D - \sqrt{\frac{e^3 F}{\pi \varepsilon_0 \varepsilon opt}} \right) \right\} \tag{10}$$

where ν is the typical phonon interaction frequency (set to a standard value of 10^{13} Hz), $\beta = \sqrt{\frac{e^3}{\pi \varepsilon_0 \varepsilon_{opt}}}$, with ε_{opt} being the optical dielectric constant (reference value: ~ 9.0 for stoichiometric Al_2O_3,[10] while ~ 6.5 for plasma-grown AlO_x dielectrics.[4] By this complete model the jV-data was fitted successfully.

III. KMC-RESULTS FOR Al/AlO$_x$/Au

A. KMC-fits to experimental JV-profiles based on AlO$_x$ defects and parameters from literature

With the kMC-simulator being validated in several studies,[19–21,40,41] we concentrate on the accurate parameterization of the model with respect to defect levels. In these terms, Matsunaga et. al. identified neutral oxygen vacancies V_O^0 in bulk α-Al_2O_3 as donors about 2.9 eV below CBM ("α" refers to the most stable hexagonal phase of Al_2O_3),[42] confirmed by Carrasco et. al. who positioned them as the dominant defect about 3.2 eV below CBM (and slightly below E_F).[38] To overcome the problems of linear density approximation (LDA) or generalized gradient approximation (GGA) in DFT, which underestimate the bandgap, Weber, Janotti and Van de Walle used GGA methods with hybrid functionals for orthorombic κ-Al_2O_3. They derived the dominant native defect levels to be oxygen vacancies in different charge states, acting as donors at $\sim 2.8 - 3.0$ eV below CBM.[43] Similarly, for α-Al_2O_3, they reported most interestingly in our terms, that V_O and Al_i are the dominant defect types located at ~ 4.1 eV and ~ 1.9 eV below CBM, respectively, and also transition levels due to Al dangling bonds at ~ 2.8 eV below CBM.[44] Most recently, Liu, Lin and Robertson provided defect levels for both orthorombic θ-Al_2O_3 and amorphous (am-)Al_2O_3, i.e. V_O^0 levels near midgap at 3.1 eV, V_O^+ 2.8 eV below CBM for θ-Al_2O_3 and V_O^0 levels in am-Al_2O_3 at 2.0 eV.[45] However, the latter value also suffered from an underestimation of the bandgap being only 6.2 eV. As we expect to get primarily amorphous alumina from our plasma oxidation process, this latter value is the most important reference here. To correct it for the underestimated bandgap, we assume to have the usually cited bandgap of 6.5 eV and linearly transform the defect level accordingly to 2.1 eV. The reported values categorized by defect types and phases differ just slightly and due to their approved methodology we considered the values by Robertson and van de Walle as the most reliable ones. The cited authors agree that electrons are localized in the V_O or Al_i defects. Thus hopping conduction via small polarons must be the correct trap-trap-transport mechanism, as outlined in the model section. Because the defect levels are the most critical parameter for the transport processes then, we performed a full parameterization of the defect values between 2.0 eV up to 3.2 eV with 0.2 eV step size in our simulations. For the next critical parameter, the trap mass, we stick to a smaller range of 0.2-0.4 m_0 at 0.05 m_0 step size, according to common literature values for Al_2O_3, like 0.25 m_0 or 0.35 m_0.[12] The same is true for the electron affinity of aluminum oxide which we assume to be $\sim 1.0 - 1.3$ eV[46] resulting into a CBO of $\sim 2.8 - 3.2$ eV to the Al cathode (work function 4.1-4.2 eV[5]) and $\sim 3.6 - 4.0$ eV to the Au anode (work function 4.9-5.0 eV[47,48]). The bandgap was set to 6.5 eV resembling a typical value for nanometer-thin am-Al_2O_3.[12,49,50] We determined the dielectric constant ε_r of a plasma-oxidized AlO_x layer with 3.6 nm thickness[51] and a capacitance of 1.68 $\mu F/cm^2$ to be 6.8. While typically a value of ~ 9.0 is cited for stoichiometric Al_2O_3,[10] our value is in good agreement with other plasma-grown AlO_x dielectrics.[4] With $\varepsilon_r = 6.8$, the thicknesses of different plasma-grown oxide layers could be estimated from CV-measurements, yielding capacitances of 0.9 $\mu F/cm^2$ and 1.04 $\mu F/cm^2$ and corresponding AlO_x thicknesses of 5.8 nm and 6.7 nm, respectively. Reference values and variation ranges of these parameters are summarized in Table I. Using this parameterization, the model could provide well matching fits to experimental jV-curves, shown in Fig. 2. It must be noted that the parameter set could be defined well without any further experimental anchor points. Nonetheless, the parameter set is in excellent agreement with cited literature values,
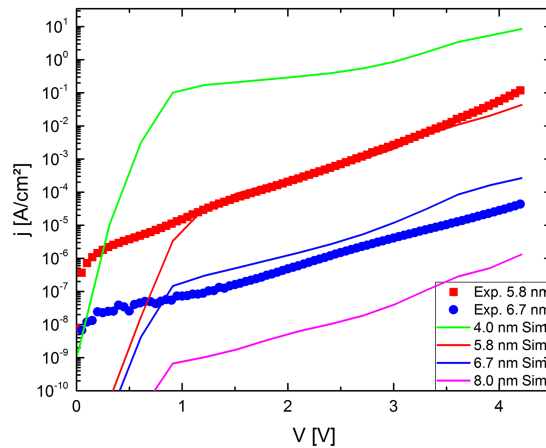
FIG. 2. Two fits to experimental curves with d_{ox}=5.8 nm (red), d_{ox}=6.7 nm (green) with *ED* deviating by 0.2 eV, plus two simulated curves with d_{ox}=4 nm (green), d_{ox}=8 nm (pink). All other parameters identical.

especially the extracted barrier height of 2.8 eV and the effective mass of 0.35 m_0. Therefore, we infer that the parabolic approximation (EMA) must be valid for the effective mass. The slight deviation of 2.8 eV barrier height from the theoretical and experimentally validated values of ~3.0 eV, would most probably vanish when using a numerical evaluation of the transmission coefficient including image forces, but the analytical computation of $T(E)$ employed by us neglects the image potential in favor of being several times faster. This offers the advantage of covering a broader parameter range without a severe systematic change of the physical processes. Moreover, our barrier height must only be increased by ~0.15 eV to obtain the "effective" value from experiments, as stated already by Weinberg earlier.[29,30] The defect density of 4×10^{18} cm^{-3} is in accordance with typical values for oxide trapped charges 2×10^{12} cm^{-2} = $(8 \times 10^{18}$ cm$^{-3})^{2/3}$ for ALD-grown AlO$_x$.[1] Considering the broadly spread values of different defect levels in Al$_2$O$_3$, we tend to attribute the defect values of 2.3-2.5 eV, extracted by us, to oxygen vacancies in am-Al$_2$O$_3$, because they stand close in energy at ~ 2.1 eV, are supposed to be dominant[45] and the plasma process is likely to form an amorphous oxide. Another possible explanation would be the forming of alumina polymorphs, including several phases of Al$_2$O$_3$, which exhibit also several energies for the dominant V$_O$ or Al$_i$, as cited above. Then the kMC-value could resemble merely a statistical average, but the implementation of several defect types would be necessary to parametrize the AlO$_x$ correctly. This would increase the parameter space to an impracticable extent. As discussed in the next section we are already able to see the relevant transport channels from the presented, sensible approximations (no image force, EMA, hopping conduction instead of multiple-phonon-ionization, just one type of defects).

B. Sensitivity of the model to the energetic shift ΔE_D and relaxation energy E_{rel}

The fits to the experimental curves, just reported, referred to a zero energetic shift of the traps, $\Delta E_D = 0$ eV, when getting occupied and a relaxation energy of $E_{rel} = S\hbar\omega = 0.4$ eV. Due to the considerable influence and high criticality of the model parameters ΔE_D and E_{rel} for the nature of defects and the results of the simulations it is important to test, how sensitive and robust the fitting results are to a variation of ΔE_D and E_{rel}. The relaxation energy $E_{rel} = S\hbar\omega$ is a characteristic property of the trap that measures the structural relaxation that accompanies phonon assisted vibrational tunneling. In such a vibrational Franck-Condon transition the Huang-Rhys factor S represents the number of phonons needed to rearrange the lattice around the final trap to accommodate a tunneling electron. Thus, phonon-assisted tunneling from a lower vibrational mode, for example the ground state, of the initial trap to a higher vibrational mode, ideally at E_{rel} above ground state, of the final trap is enabled. The process has been discussed for traps in Ref. 52 and studied computationally in Ref. 22. In case the number of involved phonons m is equal to S the multi-phonon capture (or emission) probability is maximized according to Eq. (4) (cf. also rate diagrams

in Ref. 22). To allow for this process an energetic activation barrier must be surmounted thermally. Only in case that the effective phonon number is equal to the Huang-Rhys factor, $m=S$, there is no activation barrier to be brought up, because the initial state is at the same energy as the excited vibrational mode of the final state, i.e. the energies at the respective general lattice coordinates agree (cf Ref. 22 for an energy diagram). As described in more detail in Refs. 22, 52, at elevated temperatures the current density then shows a temperature dependence at a fixed voltage, while at temperatures $\lesssim 10$ K the current density becomes temperature independent. Note again that the additional parameter, ΔE_D, reflects a separate shift in energy of the trap subsequent to the vibrational relaxation because the electron occupation number of the traps is amended during the transition process.

For the present sensitivity study $E_{D,unocc}$ was fixed to the value of the fits from Section III A, i.e. $E_{D,unocc} = 2.3$ eV for $d = 5.8$ nm and $E_{D,unocc} = 2.5$ eV for $d = 6.7$ nm. Then, three different shifts in energy from occupied to unoccupied state were simulated by varying $E_{D,occ} = E_{D,unocc} + \Delta E_D$ setting $\Delta E_D \in \{0.2$ eV, 0.4 eV, 0.6 eV$\}$. For each ΔE_D, the relaxation energy $E_{rel} = S\hbar\omega$ was set to 0.04 eV, 0.2 eV, 0.4 eV and 0.6 eV by choosing $S = 1$ and $\hbar\omega = 0.04$ eV (brown), $S = 10$ and $\hbar\omega = 0.02$ eV (green), $S = 10$ and $\hbar\omega = 0.04$ eV (magenta) and $S = 10$ and $\hbar\omega = 0.06$ eV (orange).[53] The resulting jV-profiles, presented in Fig. 3, should be compared to the measured ones and the fits with $\Delta E_D = 0$ eV (red and blue curves). This way we observed:

Firstly, in this AlO$_x$-model best fits remained for $\Delta E_D = 0$ eV and E_{rel}=0.4 eV (red and blue curves shown in Fig. 3). This could either be because dominant TAT processes are elastic ones or because the relaxation energy is relatively low or even zero in the present plasma-grown, amorphous AlO$_x$ films. Secondly, as visible for each of the two thicknesses in the two series of Fig. 3a-3c and Fig. 3d-3f with varying shift in energy ΔE_D, it holds that the larger ΔE_D is set, the stronger decreases the current density j over the whole bias range V. Also the deviation of the simulated current profiles from the experimental ones gets larger with increasing ΔE_D, particularly at higher voltages of
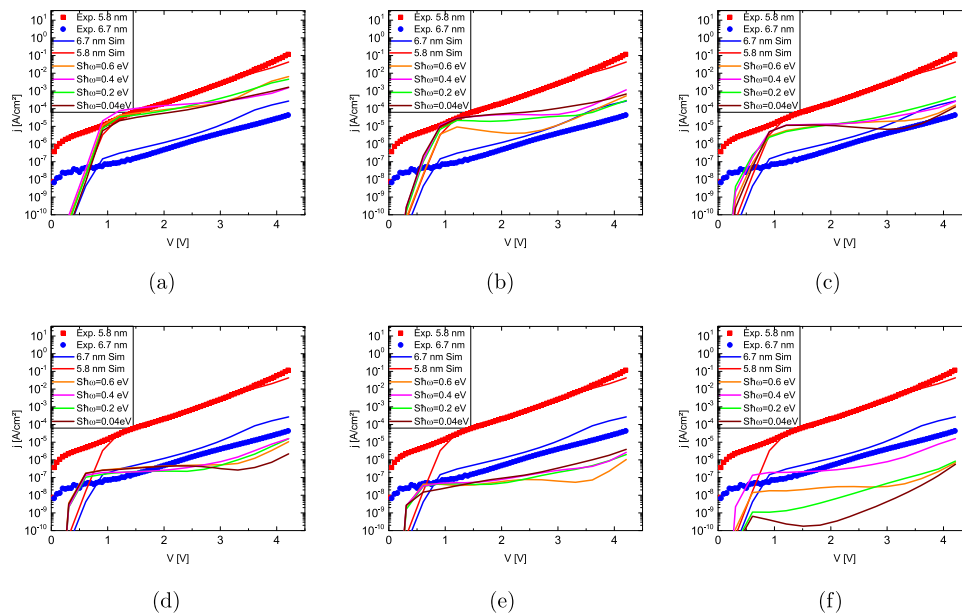

FIG. 3. Sensitivity study of the jV-profiles in dependence of a modelled shift in energy from unoccupied to occupied state ΔE_D and relaxation energy $E_{rel} = S\hbar\omega$. For both fitted AlOx thicknesses $d = 5.8$ nm with $E_{D,unocc} = 2.3$ eV and $d = 6.7$ nm with $E_{D,unocc} = 2.5 eV$ the value of ΔE_D was set to 0.2 eV in Fig. (a) and (d), 0.4 eV in Fig. (b) and (e) and 0.6 eV in Fig. (c) and (f) and for each E_{rel} the value of $S\hbar\omega$ was varied setting $S = 1$ and $\hbar\omega = 0.04$ eV (brown), $S = 10$ and $\hbar\omega = 0.02$ eV (green), $S = 10$ and $\hbar\omega = 0.04$ eV (magenta) and $\hbar\omega = 0.06$ eV (orange). These jV-profiles are to be compared with the measured ones that were fitted using $E_{rel} = 0$ eV (red and blue curves). Further discussions in the text. (a) jV-profiles, ΔE_D=0.2 eV, $d = 5.8$ nm. (b) jV-profiles, ΔE_D=0.4 eV, $d = 5.8$ nm. (c) jV-profiles, ΔE_D=0.6 eV, $d = 5.8$ nm. (d) jV-profiles, ΔE_D=0.2 eV, $d = 6.7$ nm. (e) jV-profiles, ΔE_D=0.4 eV, $d = 6.7$ nm. (f) jV-profiles, ΔE_D=0.6 eV, $d = 6.7$ nm.

$\gtrsim$ 2 V-3 V. Thirdly, the form of the experimental jV-curves is reproduced better if $\Delta E_D \gtrsim E_{rel} = S\hbar\omega$ holds. Then, the TAT-rates drop less pronounced at higher voltages going to a larger ΔE_D, e.g. from Fig. 3d to Fig. 3e with $S\hbar\omega = 0.2$ eV (green curve) or from Fig. 3b to Fig. 3c with $S\hbar\omega = 0.4$ eV (magenta curve). However, fourth, as soon as ΔE_D has surpassed $S\hbar\omega$ considerably, i.e. $\Delta E_D \approx S\hbar\omega + 0.4$ eV, the current density deviates more and more from the measured curves and from the fits for $E_{rel}=0$ eV with a further incremental step in ΔE_D of ~ 0.2 eV. This can be observed by the examples of Fig. 3e to Fig. 3f for $S\hbar\omega = 0.04$ eV (brown curves) or Fig. 3e to Fig. 3f for $S\hbar\omega = 0.2$ eV (green curves). The deviation of simulations from fits or measurements is considerably sensitive to E_{rel}, particularly for going from $S\hbar\omega = 0.04$ eV to $S\hbar\omega = 0.2$ eV. Then, for the two more moderate values of $S\hbar\omega = 0.2$ eV (green curves) and $S\hbar\omega = 0.4$ eV (magenta curves) the resulting profiles are qualitatively in better agreement with the measured curves for all tested ΔE_D and both thicknesses.

To summarize, firstly, for $\Delta E_D \gtrsim S\hbar\omega = E_{rel}$ at least the shape of measurements can be reproduced by a dominant TAT-branch. This is particularly true for larger shifts of $\Delta E_D \sim 0.4$ or 0.6 eV. Contrarily, an inacceptable discrepancy between measurements and simulations is present if $\Delta E_D \lesssim S\hbar\omega = E_{rel} \approx 0.6$ eV, but also for setting E_{rel} as small as 0.04 eV. Secondly, for small shifts $\Delta E_D \sim 0$ or 0.2 eV measured jV-curves are reproduced better in shape, if the relaxation energy $E_{rel} \sim 0.2$ to 0.4 eV (or about 0.2 to 0.4 eV larger than ΔE_D). The validity of these findings is supported by the fact that they hold independently for the two thicknesses $d = 5.8$ nm and $d = 6.7$ nm. Thirdly, we conclude from this sensitivity study that the energetic shift of the defects in these AlO$_x$ films ΔE_D is rather zero or at least very small and the relaxation energy is $E_{rel} \approx 0.4$ eV with $S = 10$ and $\hbar\omega = 0.04$ eV, since the simulated profiles are approximated best for such values. Thus, the findings on trap levels and relaxation energies in the present nm-thin, plasma-oxidized, amorphous AlO$_x$ films which were obtained by the kMC-fits in Section III A are robust and reliable. Nevertheless, it has to be pointed out that the situation in stoichiometric Al$_2$O$_3$ or crystalline or just thicker films of alumina is likely to differ from the present ones, in particular with respect to defect levels and relaxation energies, dielectric properties or dominant charge transport mechanisms.

C. KMC-parameterization of plasma-grown nm-thin AlO$_x$

In order to extract further conclusions on the simulated AlO$_x$ oxides, we proceeded with its full parameterization on the basis of the validated model. This was done with respect to its sensitivity on the most critical physical parameters, namely (in order of increasing priority) n_D, m_{ox}^*, E_B and E_D, and analyze their effects on the device performance and characteristics of the MOM-structure. Fig. 4 depicts the $j_{TAT}/j_{TOT} = j_{TAT}/(j_{TAT}+j_{DT})$, as only TAT and DT are relevant and PF-transport is irrelevant due to generally deep defect levels in AlO$_x$. If not stated otherwise, in all the plots our best fit values $n_D = 4 \times 10^{18}$ cm^{-3}, $m_{ox}^* = 0.35$ m$_0$, $E_B = 2.8$ eV, $E_D=2.4$ eV for $d_{ox} = 6.7$ nm and a typical operating voltage of 4.2 V are kept constant, apart from the parameters varied explicitly. A voltage of 4.2 V has been chosen since it is a typical value for devices and corresponds to a regime where TAT and DT rates become comparable in magnitude and competitive in kMC. In contrast, in Fig. 4a 1.2 V is used, as for such low voltages there is only TAT, while for voltages higher than 4.2 V there is only DT/FN visible.

In both Fig. 4b and Fig. 4a one can notice a clear positive correlation between E_D and E_B separating such combinations (E_D,E_B) for which TAT dominates (red) and such for which DT dominates (blue). Both show that the deeper the defects lie in the gap the higher must the barrier be to have mostly TAT as transport channel. However, for 4.2 V, Fig. 4b, the barrier value E_B must be higher than for 1.2 V to obtain a dominance of DT over TAT. This is consistent with the expectations that DT increases stronger than TAT for higher voltages. This is remarkable comparing literature values, or our fittings from Section III A, with the barrier height $E_B \approx 3.0$ eV, TAT should be dominant for the whole simulated range of operating voltages ≤ 4.2 V independent of the defect level E_D, but especially for $E_D < 3.0$ eV. So SE and DT are strongly suppressed by the high barrier between Al and AlO$_x$.

In Fig. 4c and 4d, showing j_{TAT}/j_{TOT} in dependence of (n_D, E_D) and (m_{ox}^*, E_D) for an operating voltage of 4.2 V and $d_{ox} = 6.7$ nm, other values fixed, one can see a transition from TAT to DT as soon as the dominant defect level is deeper than 3.0 eV, independent of the variable effective mass m_{ox}^* or defect density n_D, respectively. Hence, with m_{ox}^* being a material constant, as long as the defect
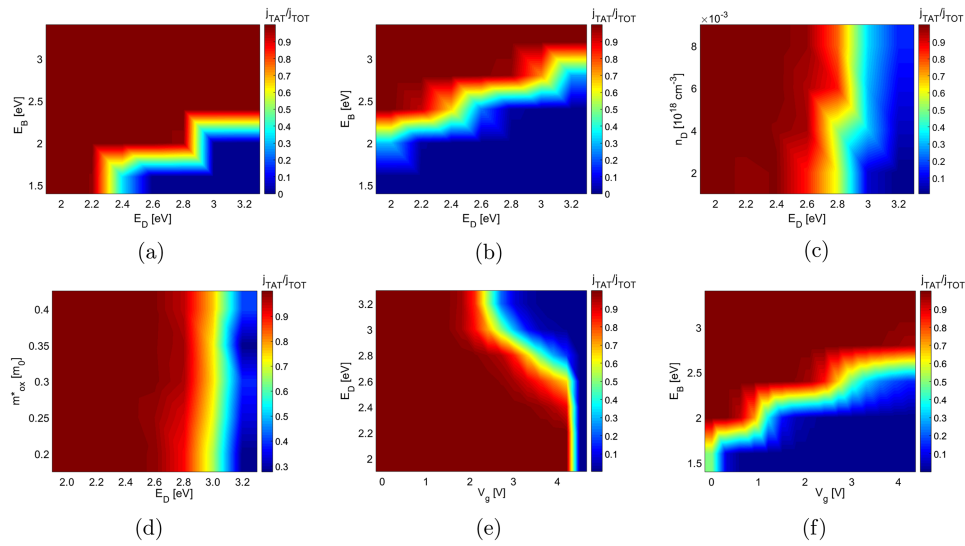
FIG. 4. Results from spanning the parameter space of Al-AlOx-Au by kMC: j_{TAT}/j_{TOT} on z-axis of plots, resembling the fraction of j_{TAT} of the total current density (maximum: 1.0, i.e. only TAT and no DT, red color; minimum: 0.0, i.e. only DT and no TAT, blue color) as well as correlations from simultaneously varying the parameters n_D, m_{ox}^*, E_B and E_D as given. Parameters not explicitly varied in a plot were set to the best fit values $n_D = 4 \times 10^{18}$ cm^{-3}, $m_{ox}^* = 0.35$ m$_0$, $E_B = 2.8$ eV, $E_D = 2.4$ eV, $d_{ox} = 6.7$ nm, $V = 4.2$ V. For further discussions see the text.(a) j_{TAT}/j_{TOT}, E_D and E_B varied, 1.2V. (b) j_{TAT}/j_{TOT}, with E_D and E_B varied. (c) j_{TAT}/j_{TOT} with E_D and n_D varied. (d) j_{TAT}/j_{TOT} with m_{ox}^* and E_D varied. (e) j_{TAT}/j_{TOT} with E_D and V varied. (f) j_{TAT}/j_{TOT} with E_B and V varied.

density cannot be driven below the relatively low values of 2×10^{18} cm^{-3}, the TAT-dominated total current in the oxide layer could only be suppressed by having only defects deeper than $E_D = 3.0$ eV present. Thus, a fabrication method providing a good crystallinity of the particular phase of Al$_2$O$_3$, is preferential.

Figure 4e and 4f depict j_{TAT}/j_{TOT} over the whole simulated voltage range in dependence of E_D and E_B, respectively. Fig. 4e confirms the evident expectation that the deeper the traps, the lower the voltage at which j_{DT} surpasses j_{TAT}, but also shows that for traps shallower than ∼2.8 eV TAT is that high that DT will become visible only for voltages above 4.2 eV. Similarly, in Fig. 4f, for barriers higher than 2.7 eV TAT is dominant for all voltages, while for lower barriers DT surpasses TAT for continuously decreasing gate voltages. Thus, both images also show a correlation separating the TAT (red) and DT (blue) dominated regimes. This implies that defects should be kept deeper than 2.8 eV, while the band offset of AlO$_x$ to the cathode should be kept higher than 2.7 eV for an optimal device operation. Additionally, one can see from Fig. 4e and 4f that independent of E_D and E_B, FN will always be dominant for voltages higher than 4.5 V.

Thus, we find that for applications that require low leakage currents (∼1 μA/cm^2), like gate dielectrics, defect densities must be minimized in the first place, because only ∼ 10^{18} cm^{-3} more defects increase TAT and thus leakage by a factor of ∼ 10. Furthermore, only if defect levels can be kept below 2.8 eV, the defect density may increase up to 8×10^{18} cm^{-3} without TAT getting dominant up to 4.2 V bias, given $E_B \gtrsim 2.8$ eV, $m_{ox}^* \gtrsim 0.35$ m$_0$ and $d \gtrsim 6.7$ nm, cf. Fig. 4c. So especially the V$_O$s around 2.8 eV are harmful in AlO$_x$. Hence, growth techniques providing good crystallinity and stoichiometry of AlO$_x$ are required to guarantee its applicability as gate dielectrics. O-rich conditions, for example, induce a Fermi-level within Al-AlO$_x$-Au-contacts that causes less rather shallow V$_O$s and Al$_{int}$s, but more deep V$_{Al}$s.[44] Thirdly, we encountered that DT/FN dominates over the trap-related processes, like TAT and PF. Also when shifting the trap energies between 2.3 to 3.2 eV at 1.2 V bias, cf. Fig 4a, or 2.0 to 3.2 eV at 4.2 V bias, cf. Fig. 4b, for a trap density of 4×10^{18} cm^{-3}, DT/FN remains dominant for a barrier $E_B \gtrsim 1.7$ eV at 1.2 V bias or $E_B \gtrsim 2.0$ eV at 4.2 V bias. Hence, concerning the magnitude of DT/FN, the barrier height is highly decisive and while the other parameters, especially the trap density, might vary more for such nm-thin, plasma-grown, amorphous AlO$_x$, the barrier height to Al, in particular, must not be

reduced below ~2.0 eV or better 2.5 eV to guarantee a low DT current for operating devices. Therefore, for example interface traps that pin the Fermi level and decrease the CBO E_B at the Al/AlO$_x$ interface must be avoided by clean processing conditions. Fourth, to keep the TAT-caused leakage current for 4-8 nm-thin gate oxides below 1 μA/cm^2, m_{ox}^* must be $\gtrsim 0.35$ m$_0$ for defect energies $E_D \lesssim 2.6$ eV and densities $n_D \sim 10^{18}$ cm^{-3}. Since such defect levels are likely in plasma-oxidized AlO$_x$, a spectroscopic determination of the effective mass in AlO$_x$ is required to evaluate its usage as a gate dielectric.

IV. CONCLUSIONS

By this extensive parameterization, we showed that our kMC-model is an accurate tool to analyze defects in oxides. It is compact and highly sensitive to physical quantities. This supports the viability of the parameter set determined by the fits and makes the kMC-model attractive to check experiments and select new measurements. We could reproduce experimental characteristics using ab initio values as input. Thus dominant defects at 2.3-2.5 eV below CBM in AlO$_x$, $m_{ox}^* = 0.35$ m$_0$ and a barrier $E_{B,Al/AlOx} \approx 2.8$ eV were extracted without image forces, or $E_{B,Al/AlOx} \approx 2.95$ eV with them. Moreover, EMA holds also in thin AlO$_x$ layers. In our seperate sensitivity study, we addressed the characteristics of defects to understand the measured jV-profiles. The variation of the two critical parameters, energetic shift ΔE_D of a trap after a transition and relaxation energy $E_{rel} = S\hbar\omega$, independently confirmed optimal fits for $\Delta E_D = 0$ eV and $E_{rel} = 0.4$ eV with $S = 10$ and $\hbar\omega = 0.04$ eV. A way higher shift $\Delta E_D \gtrsim E_{rel} \approx 0.4$ eV generated jV-curves which were at least in shape comparable to the measured ones. To derive defect parameters even more reliably, a determination of the Huang-Rhys factor S based on temperature-dependent data would be of outstanding interest in a future study. Furthermore, our model was used to predict expected electrical characteristics of ultra-thin AlO$_x$ and analyze its usefulness as gate dielectrics. We saw for $m_{ox}^* = 0.35$ m$_0$ that TAT is dominant at low bias, while FN tunneling dominates at voltages above 4.5 V. This causes dielectric breakdown, independent of defect energies $E_D \gtrsim 2.0$ eV and barriers $E_B \lesssim 3.2$ eV for $n_D \in [2\times10^{18}$ cm$^{-3}, 8\times10^{18}$ cm$^{-3}]$. Particularly, for $n_D \gtrsim 4\times10^{18}$ cm^{-3} defects and effective masses $m_{ox}^* \in [0.2$ m$_0, 0.4$ m$_0]$ and $E_B \in [2.0$ eV,3.2 eV] there will be more TAT than DT at low volts. So electrons tend to be injected from Al into AlO$_x$ defect levels and are transported via small-polaron hopping confirming ab initio predictions on AlO$_x$.[44] Hence, we suggest an optimization of the work function by minimizing interface defects to guarantee $E_{B,Al/AlOx} > 2.7$ eV and good control of bulk defects so that $E_D > 2.8$ eV and $n_D \lesssim 4 \times 10^{18}$ cm^{-3}, especially for $d_{ox} \sim 4$ nm or operating voltages $V_{ox} \gtrsim 4$ V.

[1] J. Kolodzey, A. Chowdhury, T. N. Adam, G. Qui, I. Rau, J. O. Olowolafe, J. S. Suehle, and Y. Chen, IEEE Transactions on Electron Devices **47**, 121128 (2000).
[2] K. Gloos, P. J. Koppinen, and J. P. Pekola, Journal of Physics: Condensed Matter **15**, 17331746 (2003).
[3] R. A. Johnson, P. R. De La Houssaye, C. E. Chang, P. F. Chen, M. E. Wood, G. A. Garcia, I. Lagnado, and P. M. Asbeck, IEEE Transactions on Electron Devices **45**, 10471054 (1998).
[4] K. D. Kim and C. K. Song, Applied Physics Letters **88**, 20042007 (2006).
[5] M. Bareiss, B. Tiwari, A. Hochmeister, G. Jegert, U. Zschieschang, H. Klauk, B. Fabel, G. Scarpa, G. Koblmuller, G. Bernstein, W. Porod, and P. Lugli, Microwave Theory and Techniques, IEEE Transactions on **59**, 2751 (2011).
[6] M. Barei, F. Ante, D. Ka, G. Jegert, C. Jirauschek, G. Scarpa, B. Fabel, E. M. Nelson, G. Timp, U. Zschieschang , ACS Nano **6**, 2853 (2012).
[7] B. Shin, J. R. Weber, R. D. Long, P. K. Hurley, C. G. Van De Walle, and P. C. McIntyre, Applied Physics Letters **96**, 20132016 (2010).
[8] E. J. Kim, L. Wang, P. M. Asbeck, K. C. Saraswat, and P. C. McIntyre, Applied Physics Letters **96**, 20082011 (2010).
[9] S. Nigo, M. Kubota, Y. Harada, T. Hirayama, S. Kato, H. Kitazawa, and G. Kido, Journal of Applied Physics **112** (2012).
[10] J. Robertson, Eurpoean Physical Journal Applied Physics **28**, 265291 (2004).
[11] T. Hartman and J. Chivian, Physical Review **134**, A1094A1101 (1964).
[12] M. Zemanova Dieskova, A. Ferretti, and P. Bokes, Physical Review B **87**, 18 (2013).
[13] G. Bersuker, D. C. Gilmer, D. Veksler, P. Kirsch, L. Vandelli, A. Padovani, L. Larcher, K. McKenna, A. Shluger, V. Iglesias, M. Porti, and M. Nafra, Journal of Applied Physics **110**, 124518 (2011).

[14] V. Gritsenko, K. Nasyrov, Y. Novikov, A. Aseev, S. Yoon, J.-W. Lee, E.-H. Lee, and C. Kim, Solid-State Electronics **47**, 1651 (2003), contains papers selected from the 12th Workshop on Dielectrics in Microelectronics.

[15] Y. N. Novikov, V. A. Gritsenko, and K. A. Nasyrov, Applied Physics Letters **94** (2009).

[16] H. Schroeder, S. Schmitz, and P. Meuffels, Applied Physics Letters **82**, 781 (2003).

[17] H. Schroeder, V. V. Zhirnov, R. K. Cavin, and R. Waser, Journal of Applied Physics **107**, 054517 (2010).

[18] H. Schroeder, A. Zurhelle, S. Stemmer, A. Marchewka, and R. Waser, Journal of Applied Physics **113**, 053716 (2013).

[19] G. Jegert, A. Kersch, W. Weinreich, P. Lugli, S. Member, and A. Leakage, IEEE Transactions on Electron Devices **58**, 327334 (2011).

[20] G. Jegert, D. Popescu, P. Lugli, M. J. Häufel, W. Weinreich, and A. Kersch, Physical Review B **85**, 045303 (2012).

[21] G. Jegert, A. Kersch, W. Weinreich, U. Schroeder, and P. Lugli, Applied Physics Letters **96**, 2730 (2010).

[22] L. Vandelli, A. Padovani, L. Larcher, R. G. Southwick, W. B. Knowlton, and G. Bersuker, IEEE Transactions on Electron Devices **58**, 28782887 (2011).

[23] A. Padovani, L. Larcher, G. Bersuker, and P. Pavan, IEEE Electron Device Letters **34**, 680682 (2013).

[24] A. Padovani, L. Larcher, S. Verma, P. Pavan, P. Majhi, P. Kapur, K. Parat, G. Bersuker, and K. Saraswat, 2008 IEEE International Reliability Physics Symposium, 616620 (2008).

[25] D. T. Gillespie, Journal of Computational Physics **22**, 403434 (1976).

[26] R. Tsu and L. Esaki, Applied Physics Letters **22**, 562564 (1973).

[27] By the factor m_{ca}^*/m_{an}^* in Eq. 2 the DT current could be adjusted to any other material combination.

[28] In each simulation step the homogeneous poisson equation is solved on the three dimensionally discretized simulation box which represents only the oxide.

[29] Z. Weinberg, Solid-State Electronics **20**, 11 (1977).

[30] A. Hartstein and Z. A. Weinberg, Physical Review B **20**, 1335 (1979).

[31] A. Schenk and G. Heiser, Journal of Applied Physics **81**, 7900 (1997).

[32] C. Svensson and I. Lundstroem, Journal of Applied Physics **44**, 46574663 (1973).

[33] M. Herrmann and a. Schenk, Journal of Applied Physics **77**, 4522–4540 (1995).

[34] C. H. Henry and D. V. Lang, Physical Review B **15**, 9891016 (1977).

[35] Debye temperature $T_D \approx 500K$, thus $\hbar\omega_D = k_B T_D \approx 0.04$ eV.

[36] C. Kittel, *Einführung in die Festkörperphysik* (Oldenbourg, 2006).

[37] H. Krause, Physica Status Solidi (a) **52**, 565575 (1979).

[38] J. Carrasco, J. Gomes, and F. Illas, Physical Review B **69**, 113 (2004).

[39] J. L. Hartke, Journal of Applied Physics **39**, 4871 (1968).

[40] B. Weiler, A. Gagliardi, and P. Lugli, The Journal of Physical Chemistry C (ASAP).

[41] B. Weiler, R. Nagel, T. Albes, T. Haeberle, A. Gagliardi, and P. Lugli, Journal of Applied Physics **119**, 145106 (2016).

[42] K. Matsunaga, T. Tanaka, T. Yamamoto, and Y. Ikuhara, Physical Review B **68**, 19 (2003).

[43] J. R. Weber, A. Janotti, and C. G. Van de Walle, Journal of Applied Physics **109**, 033715 (2011).

[44] M. Choi, A. Janotti, and C. G. Van de Walle, Journal of Applied Physics **113**, 044501 (2013).

[45] D. Liu, Y. Guo, L. Lin, and J. Robertson, Journal of Applied Physics **114**, 083704 (2013).

[46] J. Robertson, Journal of Vacuum Science & Technology B, 17851791 (2000).

[47] C. Erlen, P. Lugli, and S. Member, IEEE Transactions on Electron Devices **56**, 546552 (2009).

[48] C. Erlen, F. Brunetti, and P. Lugli, IEEE Proceedings on Electron Devices **78**, 36 (2006).

[49] V. V. Afanasev, M. Houssa, A. Stesmans, and M. M. Heyns, Journal of Applied Physics **91**, 3079 (2002).

[50] N. V. Nguyen, O. A. Kirillov, W. Jiang, W. Wang, J. S. Suehle, P. D. Ye, Y. Xuan, N. Goel, K.-W. Choi, W. Tsai, and S. Sayan, Applied Physics Letters **93**, 082105 (2008).

[51] U. Zschieschang, F. Ante, M. Schloerholz, M. Schmidt, K. Kern, and H. Klauk, Advanced Materials **22**, 44894493 (2010).

[52] P. F. Barbara, T. J. Meyer, and M. A. Ratner, The Journal of Physical Chemistry **100**, 13148 (1996).

[53] Since inelastic rates for MPTAT according to Eq. (4) drop exponentially as the phonon number m surpasses the Huang-Rhys factor S[22] and S was maximally set to 10, the maximum phonon number m was set to 15 in all simulations.